JOURNAL OF GEOPHYSICAL RESEARCH, VOL. 103, NO. C4, PAGES 7917–7929, APRIL 15, 1998

Tracking storm-generated waves in the northeast Pacific Ocean with ERS-1 synthetic aperture radar imagery and buoys

Benjamin Holt,[1] Antony K. Liu,[2] David W. Wang,[3] Anand Gnanadesikan,[4] and H. S. Chen[5]

Abstract. This paper examines the capability of synthetic aperture radar imagery from ERS-1 and buoys to track the wave field emanating from an intense storm over a several-day period. The first part of the study is a validation component that compares SAR-derived wave length and direction with buoy data from two locations over 10 different dates in late 1991 and National Oceanic and Atmospheric Administration (NOAA) wave model (WAM) wave direction results. When the SAR is linear (8 out of 10 cases), mean wavelength is within 5% of the buoy measurements and mean wave direction is within 1° of direction derived from the wave model (albeit with a large standard deviation of 27°), indicating close agreement. The wave field generated from the intense storm in late December 1991 was measured by three separate ERS-1 SAR passes over a 3-day period. A simple kinematic model was used for waves propagating from a storm. Comparing the model results with both SAR and buoy data indicates that SAR-derived peak wavelength and direction measurements can be reliably used to predict arrival times and propagation direction over a several-day period and considerable distances. The measurements can also be used to derive estimated wave generation source regions about the storm as well. Such measurements are useful for comparing with wave model results, which perform less accurately for direction than wave height for example, and for predicting hazardous conditions for ship navigation and coastal regions.

1. Introduction

The tracking of storms and their associated wave fields is of interest both scientifically, for understanding wind-wave generation physics and its inclusion into wave models, and operationally for monitoring potentially hazardous conditions for shipping routes and coastal environments. Early studies showed that swell could be accurately identified as emanating from storms thousands of kilometers away [*Barber and Ursell*, 1948; *Munk et al.*, 1963; *Snodgrass et al.*, 1966]. Current third-generation wave models (WAM) attempt to predict wave conditions based on integrated wind fields assimilated from satellite imagery and atmospheric soundings and much improved wind and wave physics [*Wave Model Development and Implementation (WAMDI) Group*, 1988; *Komen et al.*, 1994]. While considerable improvements have been made in predicting wave height from severe storms and rapidly rotating winds since the report by the *Sea Wave Modeling Project (SWAMP) Group* [1985], problems still exist in predicting the directional wave energy distribution. Some of these problems are due to the model resolution of propagation direction (generally 30°), which will improve with increased computer capabilities. Others are due to difficulties in determining the source regions of high storms, found to be located in the lower right quadrant of a moving storm. Waves generated from severe storms approaching landfall clearly can lead to potentially dangerous conditions for coastal inhabitants, and directional accuracy is of prime importance [*Earle et al.*, 1984; *Wang and Carolan*, 1991; *Mettlach et al.*, 1994]. The latter study evaluated both nondirectional and directional buoy spectra as well as wave model hindcasts together with a kinematic model of wave propagation to determine a possible approach for automating the estimation of the wave source regions for a large storm to help with such predictions of large waves approaching the coast. It was found that established networks of wave buoys in the northern Pacific, usually relatively close to shore, can provide valuable and near-real time data on approaching wave fields, but only under certain conditions. The use of satellite imagery especially from synthetic aperture radar (SAR) can generally improve wave directional information and prediction accuracy [*Beal*, 1991; *Komen et al.*, 1994].

Satellite imagery from SAR provides a unique two-dimensional, fine-resolution (usually 25 m) view of the ocean surface, especially waves. From this view, wavelength, propagation direction, and height information can be derived. One of the key applications of SAR has been in providing valuable information on the properties of storm-generated ocean waves. When the SAR is operating linearly over the ocean, it has been shown to provide accurate measurements on the evolution of wave fields [*Beal et al.*, 1986; *Beal*, 1991], the spatial properties of hurricane-generated waves [*McLeish and Ross*, 1983; *Holt and Gonzalez*, 1986; *Monaldo et al.*, 1993], the improvement in wave information surrounding storms compared to wave mod-

[1]Jet Propulsion Laboratory, California Institute of Technology, Pasadena.
[2]Oceans and Ice Branch, NASA Goddard Space Flight Center, Greenbelt, Maryland.
[3]Applied Technology Division, Computer Sciences Corporation, Stennis Space Center, Mississippi.
[4]Program in Atmospheric and Oceanic Sciences, Princeton University, Princeton, New Jersey.
[5]National Centers for Environmental Prediction, NOAA, Washington, D.C.

Paper number 97JC02567.
0148-0227/98/97JC-02567$09.00

els [*Beal*, 1991; *Monaldo and Beal*, 1996], and the source regions of storm-generated waves [*Gonzalez et al.*, 1987]. However, the key word here is "linear," which occurs primarily when the SAR is detecting swell or when the radar platform has a low shuttle-like orbital altitude (200–400 km). The problem is that SAR imagery of ocean waves and derived SAR wave spectra can be severely nonlinear because of the simple fact that the waves are moving at the same time the radar is precisely measuring the Doppler frequency of the moving SAR platform.

The nonlinear conditions occur primarily when waves are traveling in a direction parallel (or in azimuth traveling) to the platform flight direction. This simultaneous wave-platform motion can result in a distorted mapping of waves to imagery because the precisely timed radar returns from the waves have slightly varying Doppler frequencies and rates, termed velocity bunching. The result is either a shifting of the wave energy or actual nonimaging of wind waves moving in the azimuth direction. In addition, the SAR resolution may be degraded by coherence time limitation of the moving smaller waves [*Raney*, 1980]. Both conditions are alleviated by decreasing the ratio of the platform range-to-target compared to platform velocity. Many researchers have long sought to understand the nonlinearities sufficiently in order to correct for these by applying transfer functions [e.g., *Hasselmann et al.*, 1985; *Plant*, 1992; *Krogstad*, 1992; *Plant and Zurk*, 1997]. Understanding has progressed sufficiently to the point that SAR image spectra from the European Space Agency's ERS systems are being used reliably, albeit at considerable computational cost, in SAR wave data assimilation schemes for global wind and wave model forecasts [*Hasselmann and Hasselmann*, 1991; *Engen et al.*, 1994; *Komen et al.*, 1994; *Hasselmann et al.*, 1996].

This study examines the capability of spaceborne synthetic aperture radar imagery, obtained from ERS-1, and buoy data to track a wave field generated by an intense storm in the northeast Pacific over a several-day period. The SAR imagery and radar wave spectra were obtained from the Alaska SAR Facility (ASF) during September–December 1991. First, we establish the accuracy of the ERS-1 SAR spectra, produced by the ASF geophysical processor system (ASF GPS), for deriving the dominant wavelength and wave direction. This was accomplished by comparing 10 separate examples of SAR data nearly coincident in time and location to two sets of buoy data, one set operated by the National Data Buoy Center (NDBC) and another set deployed during a field experiment off Vancouver Island run by the Woods Hole Oceanographic Institution [*Galbraith et al.*, 1994], plus NDBC buoy-modeled wave direction from the National Oceanic and Atmospheric Administration (NOAA) wave model (WAM) [*Chen*, 1995a]. The validation segment determined that the SAR-derived dominant wave components were largely linear, which is related to the mean climatological conditions of the northern Pacific and the relative orientation of the orbital track. From this the tracking of the storm waves could proceed with some confidence. The results from the SAR wave spectra are compared with buoy data for waves generated during a storm in late December 1991. For the case study we describe a wave kinematic model, the storm, and then track the wave field over a 3-day period.

2. Data Set Description

2.1. Radar Imagery

The ERS-1 SAR imagery was acquired in the Gulf of Alaska along the general tracks outlined on Figure 1 from September–December 1991 during the 3-day repeat of the mission's commissioning phase. ERS-1 is in a Sun-synchronous orbit of about 98° and has a flight direction (azimuth angle) of about 196°T over the Gulf of Alaska during descending passes. The SAR operates at a frequency of 5.3 GHz (C band, 5-cm wavelength) over a fixed range of incidence angles from 20°–26°, which results in a swath width of 100 km. The resolution of the processed imagery is 30 m in both range and azimuth directions, and the data are formatted into 12.5-m pixels. The imagery was acquired, processed, and distributed by the ASF, which is located at the University of Alaska in Fairbanks.

The SAR wave spectra were generated from the full-resolution imagery using a wave product algorithm in the ASF geophysical processor system (ASF GPS), which also generated ice motion and ice classification products [*Stern et al.*, 1994]. The wave algorithm has been previously tested using Seasat imagery [*Wadhams and Holt*, 1991]. For each image (100 by 100 km) the wave product algorithm performs a two-dimensional digital fast Fourier transform on 16 subscenes, each 6.4 by 6.4 km in size, which are contiguous in the azimuth direction and centered along the median range line. The resulting unsmoothed spectral density estimate has a spectral resolution of $\Delta k = (1/256)\, 2\pi/25$ rad m^{-1} = 0.001 rad m^{-1} and a chi-square distribution with 2 degrees of freedom [*Monaldo*, 1991]. To reduce sampling variability, each spectrum is smoothed using a moving Gaussian filter with a full width of 21 by 21 pixels and a kernel size of 5 pixels. The smoothing increases the degrees of freedom to 164 on the basis of the effective area of the filter [*Beal et al.*, 1986]. A peak-finding routine locates the dominant local maxima or wave peaks and determines the wavelength and direction of the primary wave components by their distance and orientation from the spectra center. The radar spectra are displayed as contour plots, as seen in Figure 2a. Wave direction has a 180° ambiguity, which is generally resolved by examining weather data. For this analysis the mean and standard deviation of the wavelength and wave direction of the dominant wave peaks for a single scene are obtained from all 16 subscenes, which assumes that the wave field is approximately homogeneous over a 100-km image frame. No other corrections have been made to the SAR imagery for either system or modulation transfer functions. As further described by *Wadhams and Holt* [1991], on the basis of analysis by *Monaldo* [1991] and the characteristics of the smoothing filter the theoretical SAR wave spectral precision is ±2° in wave direction and ±0.002 rad m^{-1} in wavenumber.

2.2. NDBC Buoy Data

Wave data from three separate National Data Buoy Center (NDBC) moored buoys were utilized in this study (Figure 1). Buoys 46001 and 46003 are 6-m Navy Oceanographic and Meteorological Automatic Device (NOMAD) deep ocean buoys in the Gulf of Alaska. Data used from these buoys include wave period, significant wave height (H_s), wind speed and direction (Figure 3), and barometric pressure. All of the NOAA data used in the validation portion of the study were derived from buoy 46001 since it was closest in location to the SAR orbital tracks. A third buoy used is 46042, a 3-m coastal wave buoy which also provides wave direction. All wave data are averaged over 20-min periods. The accuracies of the wave parameters are as follows: significant wave height, ±0.2 m or 5%; wave period, ±1 s; and wave direction, ±5%.

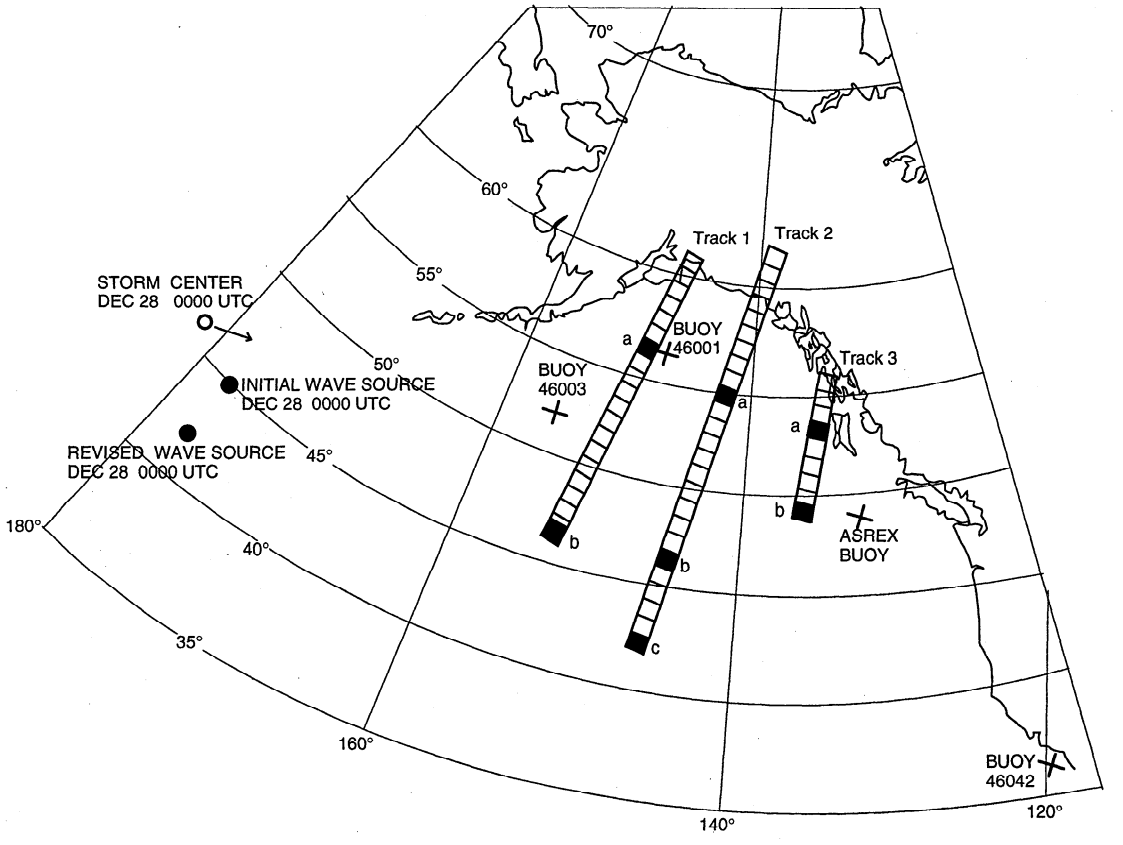

Figure 1. Map of the northeast Pacific Ocean showing the location of buoys from the National Data Buoy Center (NDBC) (46003, 46001, and 46042) and the Acoustic Surface Reverberation Experiment (ASREX) and representative synthetic aperture radar (SAR) tracks for both the validation and storm-tracking sections with solid boxes indicating SAR spectra locations.

2.3. Field Experiment Buoy Data

During the late fall and early winter of 1991 an array of buoys was deployed off the coast of Vancouver (49.2°N, 131.9°W) as part of the 1991 Acoustic Surface Reverberation Experiment (ASREX 91) (Figure 1) [*Galbraith et al.*, 1994]. Two of the moorings were waverider buoys, the first a Wavescan from Seatex AS of Norway and the other a Wavetrack from Endeco/YSI, Inc., of Marion, Massachusetts. The Seatex buoy obtains 2048 data points at 1 Hz every 3 hours, while the Endeco buoys obtained 2048 points at 2 Hz every 12 hours. The Seatex operated from November 1 to December 4, 1991, and was used in the validation segment of this study, while the Endeco buoy operated through the end of December 1991, providing data for the storm-tracking segment of the study. Also included in the mooring array was a series of meteorological measurements. A time series of wind speed and direction, significant wave height, and peak wave period derived from Seatex buoy measurements during its period of operation is shown in Figure 3.

2.4. Wave Model Data

Wave hindcast (3-hour interval) data were also obtained from the NOAA National Centers for Environmental Prediction (NCEP) using the operational NOAA WAM [*Chen*, 1995a, b; *WAMDI Group*, 1988], which provides estimates of wave direction along with the four other parameters also obtained from the NDBC deep water buoys. Wave direction from these hindcasts was used in five cases for SAR validation, supplementing the measurements from the nondirectional buoy 46001. The NOAA WAM has been used for operational forecasting since 1994 after several years of development and comparison studies with the NDBC buoy data. The model is essentially based on the cycle 4 WAM, which incorporates both wind velocity and wave age for wave generation source functions, and a quasi-linear theory of wind-wave generation [*Janssen*, 1989, 1991]. The model runs twice daily to predict global ocean wave spectra for both 12-hour hindcasts and 72-hour forecasts. The model has a grid of 2.5° in latitude and longitude. The wave spectrum is represented by 25 logarithmically spaced frequencies with the ratio of frequency increment to its frequency being equal to 0.1 and wave directionality in 30° bins. The lowest sigma layer winds from the NCEP analysis and aviation version of the global forecast system are adjusted to a height of 10 m by using a logarithmic profile [*Shearman and Zelenko*, 1989] and are used to drive the ocean surface waves. The analysis wind is for wave hindcasts, and the aviation wind is for wave forecasts.

3. Validation of SAR-Derived Wave Measurements

3.1. SAR-Buoy Comparisons

Before using the SAR wave spectra for the storm-tracking case study an assessment of the measurement accuracy of the SAR-derived dominant wavelength and wave direction was performed using comparisons with NDBC buoy 46001 and the

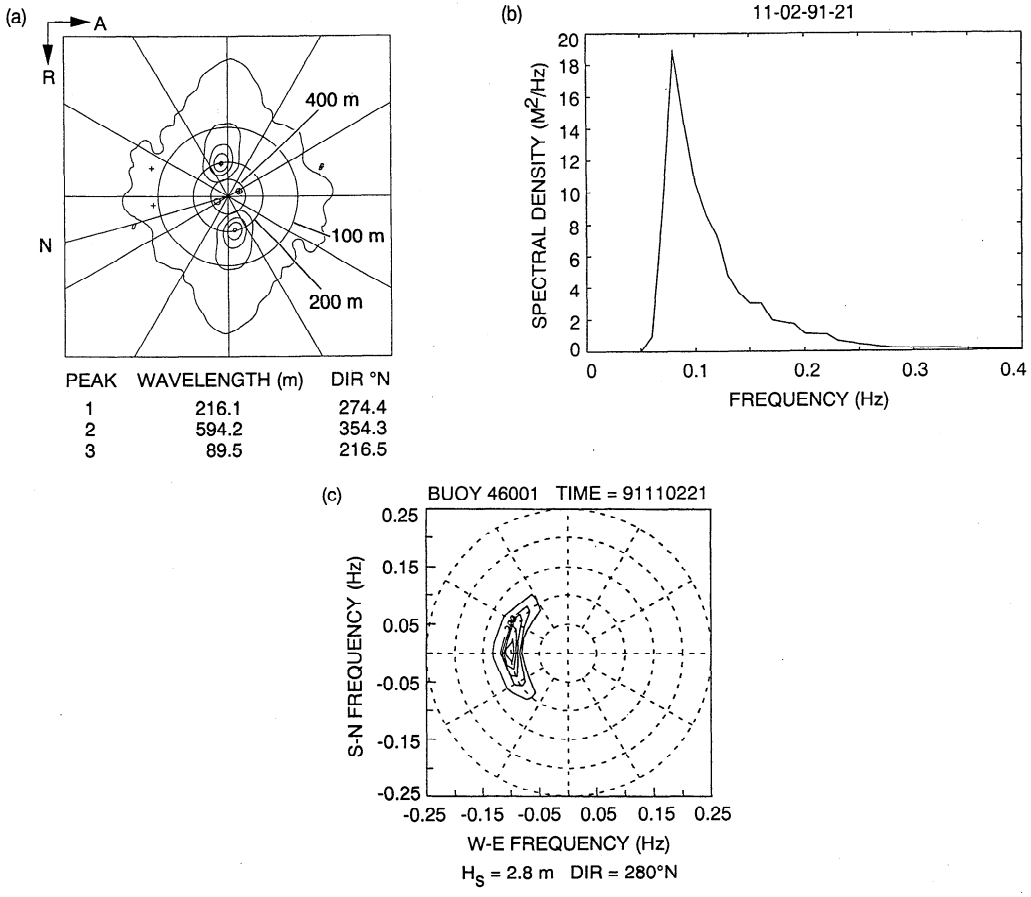

Figure 2. Comparison from November 2, 1991, at 2100 UTC of the (a) Alaska SAR Facility wave product spectrum from ERS-1 SAR and (b) buoy frequency spectrum and (c) National Oceanic and Atmospheric Administration (NOAA) wave model (WAM) results for NDBC buoy 46001.

WHOI data sets over varying environmental conditions. Ten separate buoy data sets coincident with ERS-1 SAR were utilized, five for buoy 46001 and five for the ASREX Seatex buoy. Table 1 lists the dates and time of each SAR pass. The environmental conditions for each date are detailed in Appendix A. For the comparisons with buoy 46001, buoy wave direction was derived from the WAM4 hindcasts. The SAR wave spectra were obtained from the SAR image frames closest to the two buoy locations, track 1, frame a for 46001 and, generally, track 3, frame b for Seatex (Figure 1). The distances between the buoys and the SAR frames were variable, especially for the ASREX buoys, where the closest distance was at best 135 km. The key wave parameters for the SAR and buoys are listed in Table 1. Buoy wavelength λ is derived from peak wave period T using the deep water wave dispersion relationship

$$\lambda = (T^2 g)/2\pi. \quad (1)$$

Figure 2a shows a representative SAR wave spectrum collected on November 2, 1991, which has a dominant wavelength of 216 m and propagation direction from 274°. The frequency spectra from buoy 46001 is shown in Figure 2b and the hindcast results of the NOAA WAM are shown in Figure 2c. The buoy results show the dominant wave period of about 12.4 s (0.081 Hz), corresponding to a wave length of 239 m, and the WAM results show a propagation direction from 280°. For the dominant peak wave component the SAR spectrum compares reasonably well with the buoy results; however, the SAR spectral shape is slightly distorted in the azimuth direction by the radar transfer function as compared to the model results.

Referring back to Table 1, it can be seen that of the 10 cases, 8 comparisons between the SAR measurements and the buoy measurements are favorable, while 2 cases, October 15 and November 16, show considerable differences in wavelength and wave direction. We believe these differences are due to nonlinearities in the SAR spectra resulting from azimuthal distortion and so are not considered in the following error calculations (more discussion below). Figure 4 shows the comparison of the eight linear peak SAR-derived wavelengths and buoy wave periods using the dispersion relation (1). Here we see that the SAR-derived wavelengths follow the relation but are slightly underestimated.

For the eight cases the mean fractional difference in wavelength is -5.1% with a standard deviation of 9.6%, and the mean difference is -22 m with a standard deviation of 31 m. Using the wavenumber precision of 0.002 rad m^{-1} [*Monaldo*, 1991] over the approximate range of measured buoy wavelengths (100–600 m), the theoretical accuracy in the wavelength measurements are between 3 and 20%, respectively. This average compares well with the mean absolute difference of 9.6% (29.4 m), as does the range of accuracies over the wavelength spread, since the largest discrepancies between buoy and SAR are generally those cases with the longest wavelengths. For direction the mean difference is $-0.8°$ as compared with the theoretical error of $\pm 2°$ [*Monaldo*, 1991], but

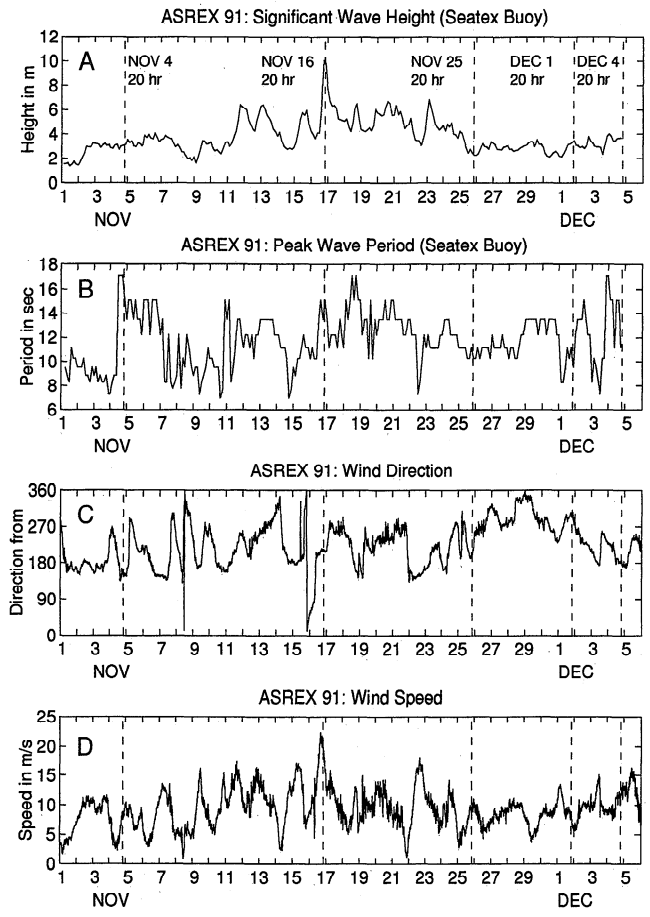

Figure 3. A time series from the ASREX Seatex buoy showing (a) significant wave height H_s, (b) peak wave period T, (c) wind direction, and (d) wind speed from November 1 to December 5, 1991. The times of the five coincident SAR data are indicated by vertical dashed lines.

there is a wide standard deviation of 27.5°. Most of the differences in direction arise from the single data point for the storm in late December, which is the storm discussed in the case study. From these two assessments the mean errors in wavelength and wave direction fall within the expected ranges when the SAR wave spectra are linear.

To assess the tendency of the SAR spectra to be linear or nonlinear in the case of the two unfavorable measurements, we use the velocity bunching parameter,

$$C = (1/4)(R/V)H_s g^{1/2} 2\pi\lambda^{-3/2} G(\theta, \phi) \cos\phi \qquad (2)$$

where R is slant range from radar to the surface, V is platform velocity, H_s is significant wave height, g is the gravitational constant, and G is the platform and ocean wave geometry (θ is radar incidence angle and ϕ is the azimuth angle between the platform and wave direction) [*Alpers*, 1983]. Significant nonlinearities occur if $C > \pi/2$, indicating that shifts of spectral peaks toward lower wavenumbers are likely to occur. More specifically, nonlinear mapping results from a surface scatterer having a velocity component radial to the SAR look direction. The resultant displacement of the scatterer on the SAR image is in the azimuth or along-track direction (in all cases the spacecraft heading is about 195°T). Random shifts cause the image to be smeared in the azimuth direction, which causes a decrease in response for high-azimuth wavenumbers in the image spectra. For ERS-1 the R/V ratio is about 115 s. As shown in Table 1, values of C near 2 or greater are obtained for the two nonlinear cases on October 15 and November 16 because of the comparatively short wavelength and large H_s in both cases. The remaining eight cases have values generally much less than 1.5. The one other case with azimuth-traveling waves, October 24, shows reasonable comparisons in wavelength and wave direction or no obvious distortions in the wave spectra, despite a generally high C value.

Table 1. Comparison of SAR and Buoy Wave Parameters

						SAR Data			Buoy Data						
Buoy	Track	Position	Date	Time, UTC	Distance, km	SAR λ, m	SAR Direction, deg	C	T, s	λ, m	Direction, deg	H_s, m	U, m s^{-1}	Δλ, %	Δdirection, deg
46001	1	a	Sept. 18	2100	58	179	252	1.09	11	189	230	3.0	8	−5	22
46001	1	a	Oct. 15	2100	38	157	265	2.28	10	156	140	4.0	12	...	...
						196	134								
46001	1	a	Oct. 24	2100	38	103	195	1.39	8.3	107	180	1.0	4	−4	15
46001	1	a	Nov. 2	2100	25	216	274	0.21	12.4	239	280	4.5	8	−10	−6
46001	1	a	Dec. 29	2100	25	565	240	0.22	20.0	624	300	6.0	14	−10	−60
Seatex	3	b	Nov. 4	2000	198	327	261	0.25	15.7	383	264	3.1	8	−15	−3
Seatex	3	a	Nov. 16	2000	228	195	288	1.97	14.6	332	238	10	21	...	...
						536	175								
Seatex	3	b	Nov. 25	2000	135	175	307	0.24	10.3	164	278	2.3	8	7	29
Seatex	3	b	Dec. 1	2000	135	182	291	0.02	10.3	164	286	3.4	5	11	5
Seatex	3	b	Dec. 4	2000	202	296	273	0.08	15.0	350	281	3.5	8	−15	−8
Mean Δ														−5.1	−0.8
Standard deviation														9.6	27.5
Mean absolute Δ														9.6	18.5
Standard deviation														4.1	19.1

Track and position are of the SAR image, see Figure 1; Distance is from the buoy to the SAR image; SAR λ is the SAR-measured wavelength of dominant peak; SAR Direction is the SAR-measured dominant peak wave direction from source; C is the velocity bunching parameter, reference is *Alpers* [1983]; T is the buoy peak wave period; λ is derived from T using dispersion relationship (1); Direction is the wave direction from source, derived from NOAA/WAM hindcast; H_s is the significant wave height; U is the wind speed; Δλ is the fractional difference in wavelength between buoy and SAR; and Δdirection is the difference in wave direction between buoy and SAR. ERS-1 flight (azimuth) direction is 196°T for all images. For Seatex direction, 21° are added for magnetic correction. NDBC 46001 location is 56.3°N, 148.3°W. WHOI ASREX Seatex location is 49.15°N, 131.89°W.

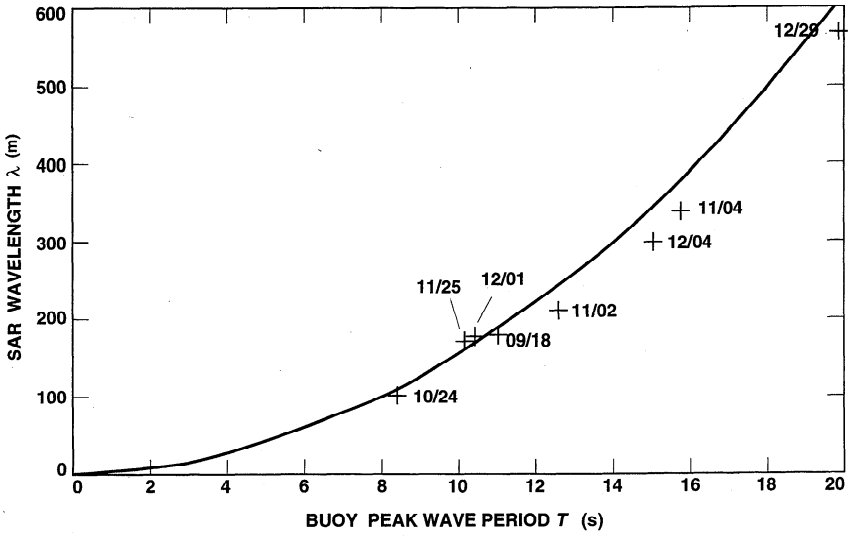

Figure 4. Comparison of measurements of peak wave period from buoy 46001 and the Seatex buoy with wavelength from ERS-1 SAR derived using the wave dispersion relation (1). See Table 1 for details.

3.2. Comparison With Other SAR Wave Validation Studies

During the early months of ERS-1 in 1991 several validation campaigns took place to assess the capability of the SAR for generating useful wave information. The Grand Banks validation program, summarized by *Dobson and Vachon* [1994], had the following key results: ERS-1 SAR accurately measured long wavelength swell, the SAR did not measure any azimuth-traveling waves shorter than 200 m, but range-traveling waves were measured as short as 50 m [*Vachon et al.*, 1994]. For the winter conditions seen in the Grand Banks area, a majority of the SAR acquisitions were obtained of azimuth-traveling waves. Quasi-linear remapping was more effective than nonlinear remapping to invert the problematic SAR spectra [*Krogstad et al.*, 1994]. SAR and wave models were found to be complementary, since SAR was best at mapping swell and the wave model was best at mapping wind seas. Similar results were found in other validation experiments [*Kleijweg and Greidanus*, 1993; *Tilley and Beal*, 1994]. These results were essentially as predicted, based on years of analysis using SAR imagery from satellite, shuttle, and airborne platforms. To make full use of the ERS-1 SAR wave mode data, where small 5-km vignettes are sampled every 100–200 km on a global basis, a nonlinear inversion algorithm has been developed, where the SAR spectra are remapped in an iterative fashion together with WAM [*Hasselmann and Hasselmann*, 1991]. Results indicate that this is effective in producing accurate measurements of wavelength and wave direction as well as height [*Komen et al.*, 1994].

3.3. Validation Summary

This validation component showed that SAR wave spectra derived using a simple filter and no transfer functions were found to be reasonably accurate in measurements of peak wavelength and wave direction. This was largely fortuitous because of the meteorological conditions found in the northeast Pacific at least during the months September through December 1991, when west to east swell (or range-traveling swell relative to the ERS-1 flight direction) was predominantly measured, and, hence, accurately mapped onto the SAR wave spectra. This dominant weather pattern is attributed to the semipermanent Aleutian Low, which is particularly intense during these early winter months [*Overland and Heister*, 1980]. One circumstance, on October 24, did accurately measure short, azimuth-traveling waves, presumably due to the low wave height. The two cases where comparisons with buoy data were poor, October 15 and November 16, were due to the presence of variable wind seas and the proximity of the buoy to the storm center, respectively. Another case, in late December, resulted in large differences in wave direction, likely due to difficulties in modeling directional data from large storms, as will be discussed in the next section. Thus, under favorable conditions, these products can be reliably used for further investigations in this general region.

4. Case Study of Storm and Swell Evolution

In this section we examine the evolution of swell across the northeastern Pacific generated by a storm using SAR, buoys, and a kinematic wave model. The data set was identified by the fortuitous combination of a strong low-pressure system, suitable SAR coverage of the emanating wave field, and buoy data both from NDBC and ASREX. We use a simple kinematic model derived by *Gonzalez et al.* [1987] for comparison with the various buoy wave measurement sources. The synoptic weather chart of the storm on December 28, 1991, at 0000 UTC is shown in Figure 5, and a location map of the ERS-1 SAR tracks and buoys is shown in Figure 1.

4.1. Kinematic Wave Model

Using SAR wave spectra of a hurricane-generated wave field obtained from a shuttle-based (and hence lower-altitude) platform and a simple kinematic wave model, *Gonzalez et al.* [1987] have shown that swell generally obeys the linear wave theory of propagation and does not seem to be affected by propagation through zones of steady wind. It is assumed that the waves originate from approximately a point source or a generation region sufficiently far away to be considered as a point source. Swell (wavenumber k) generation is defined as that point when the deep water group velocity

$$C_g = 1/2(gk)^{1/2} \tag{3}$$

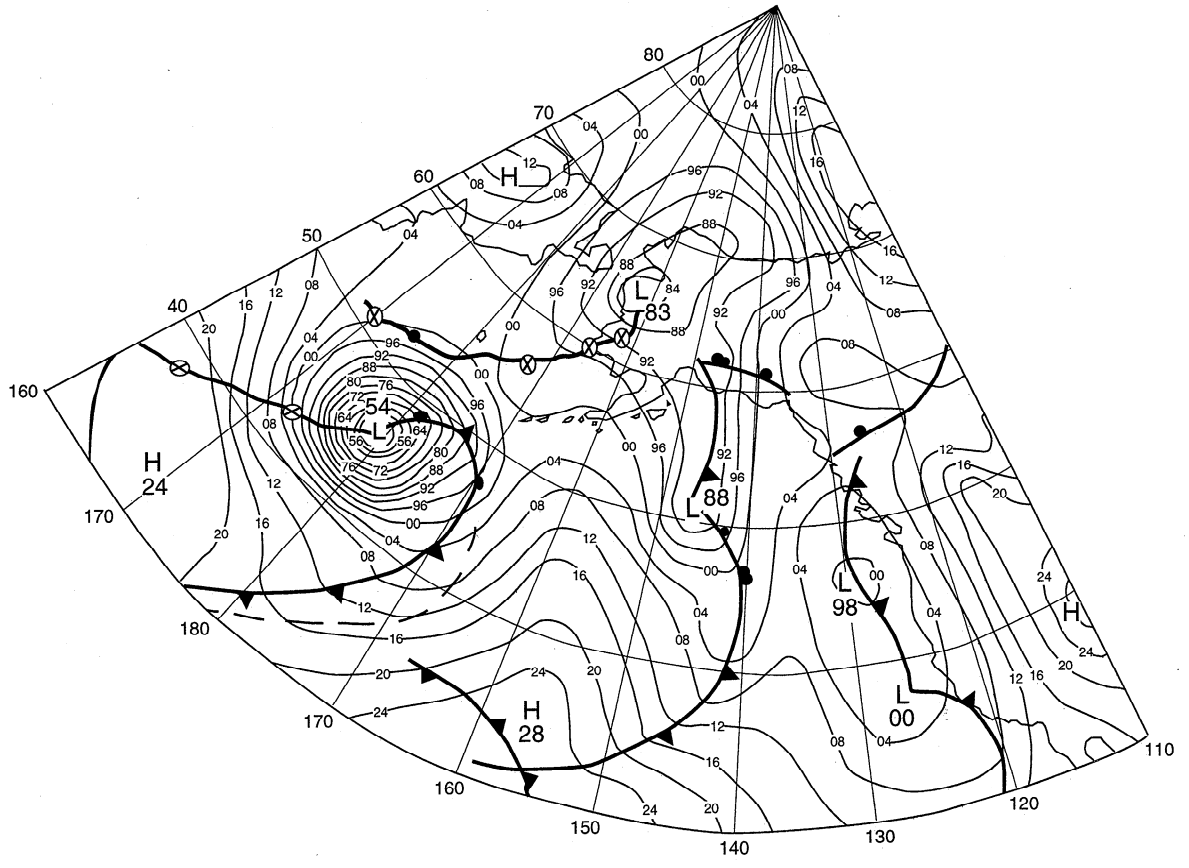

Figure 5. National Climatic Data Center (NCDC) surface analysis synoptic weather chart at 0000 UTC on December 28, 1991. The low-pressure region (954 mbar) identifies the storm used in this study.

exceeds the local wind speed component in the wave direction. The wave then ceases to be forced by the wind and begins to propagate freely as swell. By assuming such a swell system consists of free waves and is unaffected by other processes, such as wave-wave interaction and wave-current interaction, the swell directions at distant locations can be checked with the linear wave propagation model.

The geometry of the idealized storm swell kinematic model is shown in Figure 6 with the position of S (ϕ, λ) being the center of the swell generation region and P and C being observation points. The great circle distance s to an observation point is given by *Snyder* [1987] to be

$$\sin = [\sin^2 + \cos \phi_s \cos \phi_p \sin^2]^{1/2}, \quad (4)$$

where s is the radian measure of the great circle distance. The wave propagation direction or azimuth angle B_p at an observation point is found by combining two angles. The first angle θ_p is the internal angle subtended by two great circles, one that extends through S and P and the other that extends through P and C. The second angle θ_r is the azimuth angle from P to C (SAR path). Spherical geometry (Figure 6) then determines the following relationships:

$$\theta_p = \cos^{-1} \quad (5)$$

and

$$s = C_g(t_p - t_s) \quad (6a)$$

$$l = C_g(t_c - t_s). \quad (6b)$$

In these relationships, if the quantities of (ϕ, λ), C_g, and t_s are assumed to be known, then (4), (5), (6a), and (6b) can be solved for the swell propagation direction B_p and arrival time t_i for locations P and C.

4.2. Wave Data Comparison

4.2.1. Storm description. According to the surface synoptic weather analysis [*National Oceanic and Atmospheric Ad-*

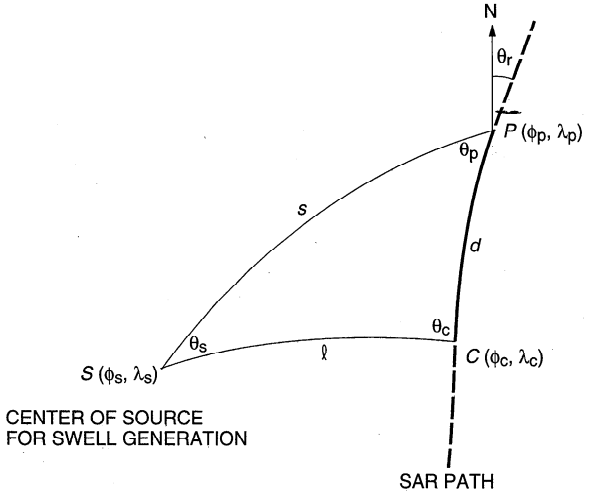

Figure 6. Geometry of the idealized storm swell kinematic model. The point S represents the source of swell generation, and P and C are points of SAR imaging locations.

Table 2. Storm-Tracking Wave Data

Buoy	SAR Orbit	Track	Position	Location: Latitude, °N	Location: Longitude, °W	Date	Time, UTC	Distance S, km	B_p, deg	Direction, deg	λ, m	H_s, m	C_g, km h^{-1}	T_{C_g}, hour	ΔT, hour
NDBC 46003				51.9	155.9	Dec. 29	1000	1723	···	···	624	7	56.1	30.7	34
NDBC 46001				56.3	148.3	Dec. 29	2200	2351	···	···	624	6	56.1	41.9	44
	E2376	1	a	56.2	149.8	Dec. 29	2100	2260	250	240	565	···	53.4	42.3	45
	E2376	1	b	46.6	153.3	Dec. 29	2100	1835	264	265	388	···	44.0	41.7	45
Endeco				49.1	131.8	Dec. 30	1200	3395	···	···	624	4	56.1	60.5	60
	E2390	2	a	54.7	142.0	Dec. 30	2000	2698	263	253	373	···	43.4	62.2	69
	E2390	2	b	47.0	144.8	Dec. 30	2000	2479	278	267	316	···	40.0	62.0	69
	E2390	2	c	43.2	145.9	Dec. 30	2100	2476	286	288	317	···	40.5	61.8	69
Endeco				49.1	131.8	Dec. 31	0000	3395	···	···	433	6	46.8	72.5	72
NDBC 46042				36.8	122.4	Dec. 31	0600	4588	···	300	624	5	56.1	81.8	82
	E2404	3	a	53.5	134.2	Dec. 31	2000	3192	···	266	292	···	38.4	83.1	92

Buoy is the buoy identifier, the Endeco buoy is located at ASREX site on Figure 1; SAR Orbit (with Track and Position) is the ERS-1 (E) orbit number plus track and position of the SAR image on Figure 1; Distance S is the great circle distance from the initial estimated storm wave generation region (45°N, 177°W) to the SAR image or buoy position using (4); B_p is the great circle angle of wave propagation direction using (5); Direction is the direction from which waves are propagating measured from SAR or buoy spectra; λ is the peak wavelength measured directly from SAR spectra or derived from the buoy-measured peak wave period using the dispersion relation (1); H_s is the significant wave height measured from buoy; C_g is the group velocity derived from SAR or buoy measurement of wavelength or period; T_{C_g} is the hours of wave travel time using C_g and distance S; ΔT is the time difference between the estimated storm wave generation time (December 28, 0000 UT) and buoy or SAR wavelength measurement. B_p for E2404 was not derived since there are only two of three points for (5).

ministration, 1992] a low-pressure system developed near Japan on December 25, 1991, and moved rapidly eastward. By December 27, at 1200 UTC, it was a 962-mbar storm near the international date line. At 0000 UTC on December 28 the intensive storm had matured to a center pressure of 954 mbar and was moving northeastward (about 60°) to a position of about 46°N, 179°E (Figure 5). The storm had started to weaken, and its forward speed began to decrease by 0000 UTC on December 29. Using the general concept that a storm's most intense wind and wave generation zone is the lower right quadrant with respect to the storm's path, this would place the intense wave generation zone on the southeast side of the northeast traveling storm. The center of this swell generation zone is initially estimated to be 45°N, 177°W on the southwest side of the center of the storm, some 300 km distance from the storm center (Figure 1). Since the swell generation zone and time can be shifted for various propagation directions within the storm's southeast quadrant, the postulated zones and time can be fine-tuned through iteration.

4.2.2. SAR data. Data from three ERS-1 SAR acquisitions along descending orbits were obtained on December 29, 30, and 31, 1991. Six SAR wave spectra were processed, at positions selected to sample the spreading of the wave field as well as to be close to the buoys (Figure 1). The dominant wavelength and wave direction from these spectra are listed in Table 2, and representative spectra from December 29 are shown in Figure 7. In all cases the wavelengths are >300 m, and the wave directions are eastward or range traveling with respect to the satellite track. No nonlinear mapping is apparent in any of the spectra. The longest waves (565 m) are from the northernmost spectra on December 29. As the available SAR data progress to the east and move later in time, wavelength decreases but wave direction maintains a general clockwise rotation from north to south. This is seen at position a on the three tracks (240°, 253°, and 266°), indicating the rotational spread of the wind source. Position b on Tracks 1 and 2 have nearly the same wave direction (265° and 267°) while being 23 hours apart, indicating that the locations of these images are well aligned with the wave propagation direction.

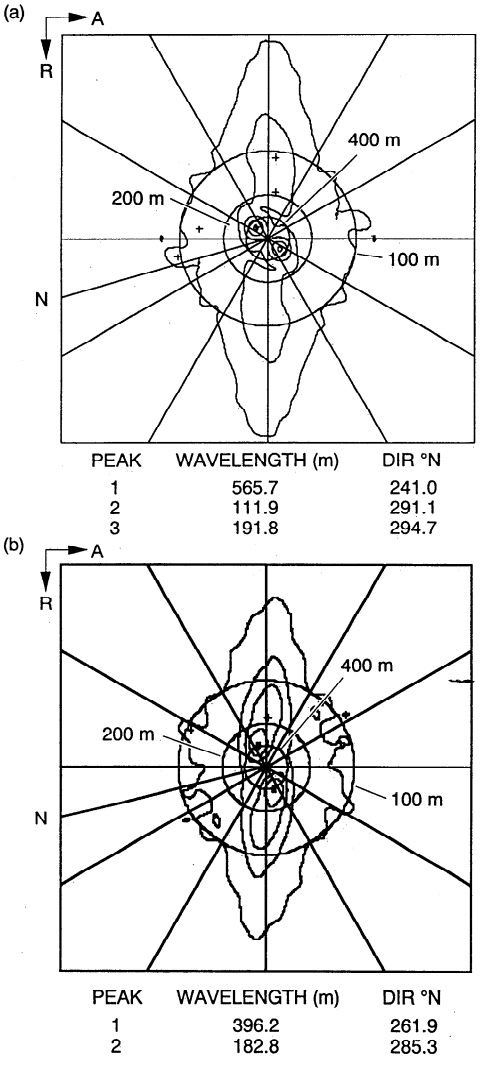

Figure 7. Alaska SAR Facility wave products of ERS-1 SAR spectra from December 29, 1991 (E2376), in the northeast Pacific from (a) track 1, frame a and (b) track 1, frame b (see Figure 1).

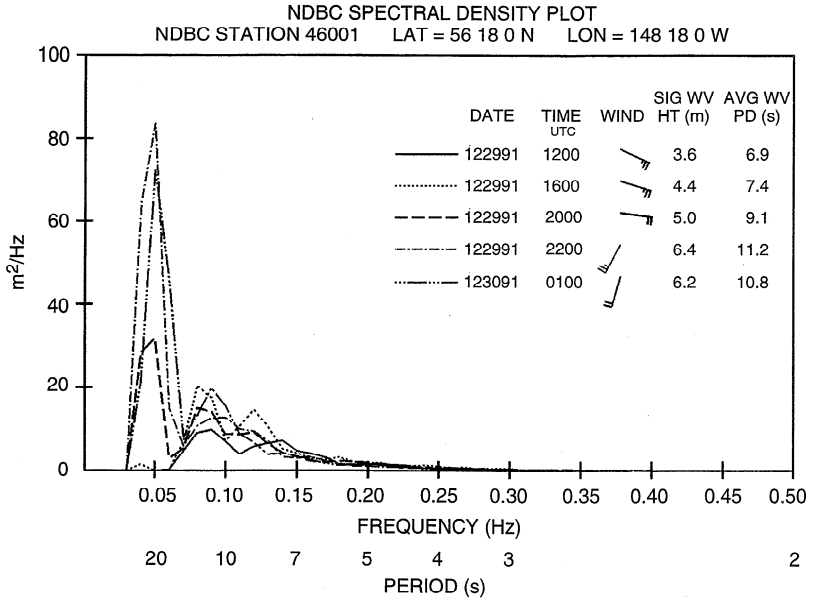

Figure 8. Time series of wave spectra from NDBC buoy 46001 on December 29, 1991.

4.2.3. Buoy wave data. For this study, NDBC buoys 46001, 46003, and 46042 have been utilized, noting again that 46042 is a directional buoy. From the WHOI ASREX program, data from the nondirectional Endeco buoy was used, since the directional Seatex buoy had already been recovered. Table 2 lists the key buoy information.

For buoy 46001 the low-frequency peak of 0.05 Hz reached a maximum density and wave height of more than 6 m on December 29 at 2200 UTC (Figure 8), very close in time and position to the nearest SAR wave spectra. The contour plots for buoys 46001 and 46003 (Figure 9) show clearly the arrival of the 0.05-Hz peak at 46003 to be about 11 hours earlier than at 46001 because of its closer proximity to the storm center. This peak persisted at each buoy for at least 6 hours after arrival (Figure 10). The Endeco buoy showed the arrival time of the wave peak at 1200 UTC on December 30 and a significant decrease in period 12 hours later. At buoy 46042 the same low (0.05 Hz) wavenumber peak arrived on December 31 at 0600 UTC, persisting for some 12 hours with a direction from 300° (Figure 11).

4.2.4. Data comparisons. It is clear from the buoy and SAR results that the peak storm wave field was captured at all four buoys at successive times and at least at the northernmost image from E2376. The remaining SAR frames sampled the storm waves after the wave field maximum had already passed through. This is primarily due to the sampling rate of the satellite being less than fortuitous (no ascending passes were acquired, for example, which are separated in time from the descending passes by about 12 hours). The southernmost image of E2376 had a shorter wavelength (388 m) than might be expected since it was only about 400 km to the south of its companion wave field, which measured over 550 m in wavelength. The smaller measurement may be caused by a slightly less favorable generation direction, which was not as parallel to the storm isobar contours. In terms of direction the southerly end of E2390 and buoy 46042 had similar directional measurements for the peak wave field 9 hours apart.

4.3. Data-Model Results and Discussion

First we consider the arrival times measured by the group velocity derived from the SAR and buoy measurements (T_{c_g}), compared with the total elapsed time (ΔT) between the observations and the estimated storm source time (December 28,

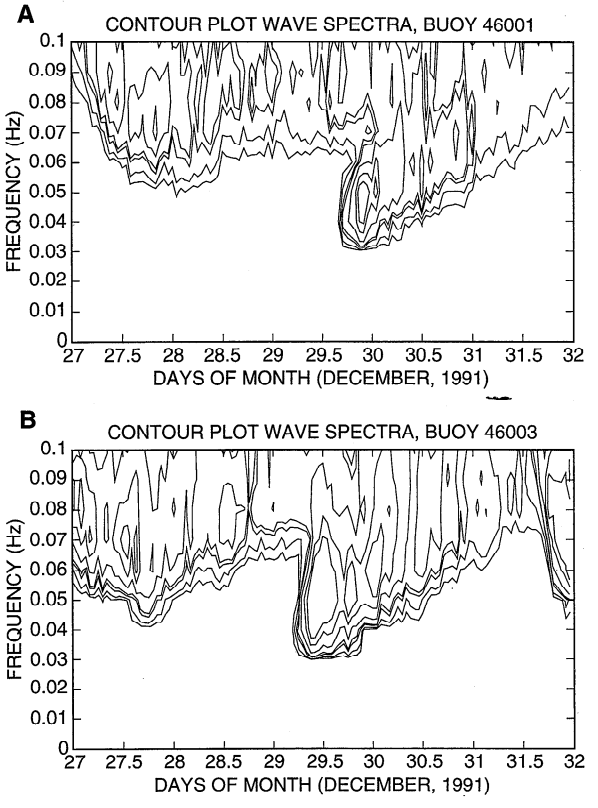

Figure 9. Contour plots of wave spectra from (a) buoy 46001 and (b) buoy 46003 during December 27–31, 1991.

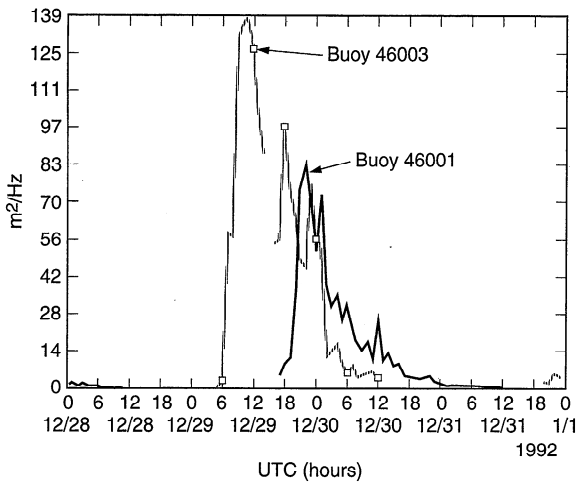

Figure 10. Time series plot of peak wave spectral density for (a) buoy 46001 and (b) buoy 46003 during December 28–31, 1991.

0000 UTC). It can be seen from Table 2 that by and large these measurements result in earlier arrival times, with the exception of the most distant buoy measurements (Endeco and 46042), where the derived arrival times are nearly equal to the elapsed times. The earlier times would indicate that the estimated source region needs updating by being moved farther away, but the close times of the distance buoys suggest that the estimated source location and time is actually quite good.

The comparisons of direction estimated by the model results (B_p) with the SAR measurements are generally favorable. We see that the two southernmost measurements are nearly the same, while the remaining three northerly SAR measurements are 10° less (or rotated counterclockwise) from the model. The differences may be due to wave-current refraction as the wave field passes through the Alaskan Coastal Current. This small set of measurements does suggest that this simple kinematic model is adequate for describing the general fan-shaped directional wave information from a strong storm.

Next, we use the SAR directional measurements to iterate the storm wave generation zone. This can be done simply by adding the equivalent distance ΔS based on C_g for the difference in time between T_{C_g} and ΔT for each measurement (Table 3). Using (4), revised source regions are calculated for the six measurements, which results in an updated mean position of about 42°N, 177°W, ~475 km from the storm center (46°N, 179°E) as compared to 300 km with the first estimated point source (45°N, 177°W) (Figure 1). Using the revised point source, we then recalculate T_{C_g} for the four buoys ($^*T_{C_g}$ in Table 3), showing closer comparisons with ΔT. The revised source region is moved farther back into the lower right quadrant with respect to storm travel (about 60°). These results indicate that the peak waves were generated within a few hours of the original estimated time that the storm reached its lowest pressure (December 28 at 0000 UTC) and from a region some 300–500 km to the lower right of the storm with respect to its travel direction. This is compared to previous results from *Gonzalez et al.* [1987] showing waves being generated within 200–300 km of a hurricane center, a radius greater than expected from the generally 50–100-km radius of maximum hurricane winds. The larger radius for this Pacific storm is still contained within the tight isobars seen on Figure 5. *Mettlach et al.* [1994] found differences of 5° in latitude and 4° in longitude in estimates of the wave source region about a typhoon using several methods, which are comparable to these results.

5. Summary

This study indicates that the dominant wavelength and wave direction from SAR measurements plus a simple kinematic model can be used to provide useful information on the wave field emanating from strong storms. Taken separately, the SAR spectra from either E2376 and E2390 provides sufficient details to enable some predictive capability for determining the arrival time, energetics, and direction of large swell propagating from remote storms toward coastal areas. Samples from multiple SAR passes improve this predictive capability. The SAR directional information in particular can enhance both buoy data and wave model results as well as provide improved information on the wind fields from storms, including estimating the source region and generation time.

A key to using SAR for such studies and especially in an operational application is adequate sampling. Spaceborne SAR is either data-rate limited or power limited, which prevents duty cycles (amount of time that the SAR can operate) greater than about 30%. The ERS SARs operate outside ground reception stations in its unique wave mode, producing 5-km vignettes every 200 km along-track. This is potentially a very useful mode except that the data are stored on board and downlinked to a ground station when possible. This delay is at least 90–100 min or as much as several hours depending on how often the satellite comes into view per day of a ground station designated to receive such data. Also, the spectral products from these vignettes are not yet operationally available. Spaceborne SARs have 14–16 orbits per day and limited swaths compared to operational sensors such as AVHRR. Options therefore for improving coverage are to increase swath width (usually at the expense of resolution, which is particularly important for wave imaging on SAR), such as with Can-

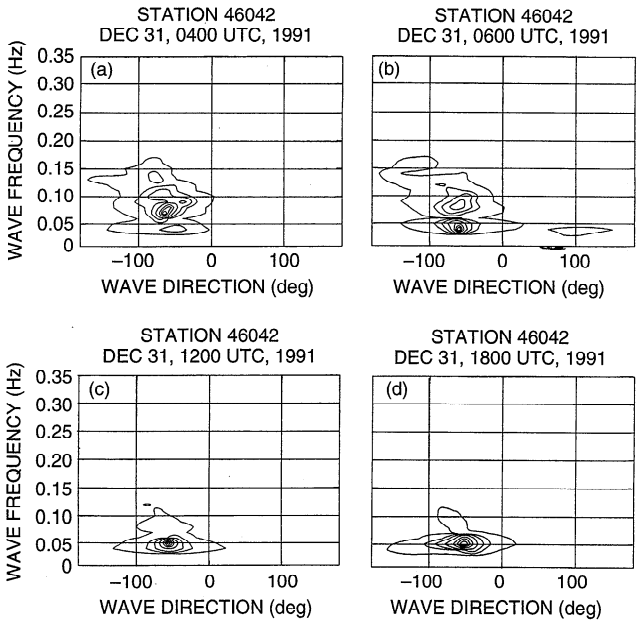

Figure 11. Directional wave spectra from buoy 46042 near Monterey, California, at (a) 0400, (b) 0600, (c) 1200, and (d) 1800 UTC on December 31, 1991.

Table 3. Revised Storm-Tracking Wave Data

Buoy	SAR Orbit	Track	Position	Distance S, km	Direction, deg	C_g, km h^{-1}	$T_{C_g} - \Delta T$, hour	ΔS, km	Latitude, °N	Longitude	$^*T_{C_g}$, hour	ΔT, hour
	E2376	1	a	2260	240	53.4	2.7	144	42.1	175.3°W		
	E2376	1	b	1835	265	44.0	3.3	145	42.3	177.7°W		
	E2390	2	a	2698	253	43.4	6.8	273–295	40.8	176.6°W		
	E2390	2	b	2479	267	40.0	7.0	260–280	40.5	178.0°W		
	E2390	2	c	2476	288	40.5	7.1	271–288	45.7	179.4°E		
	E2404	3	a	3192	266	38.4	8.9	342	41.4	179.7°W		
NDBC 46003											34.4	34
NDBC 46001											46.2	44
Endeco*											63	60
NDBC 46042											82.8	82

$T_{C_g} - \Delta T$ is the travel time difference from Table 2; ΔS is the change in kilometers from $(T_{C_g} - \Delta T)C_g$; Latitude and Longitude give the revised storm wave generation source region based on Direction and ΔS; $^*T_{C_g}$ is the revised hours of wave travel time using C_g, Distance $S + \Delta S$, and mean of revised latitude and longitude (42°N, 177°W). See footnotes to Table 2.

*Date is December 30, and time is 1200 UTC.

ada's RADARSAT, or to use multiple satellites placed in orbits 1–2 days apart in their repeat pattern, such as ERS-1 and ERS-2 recently were in their tandem phase. Also, of key importance is to get rapid data reception, processing, and incorporation of results with wave model and buoy data. The real-time SAR ocean wave spectra processor flown on two shuttle flights in 1994 demonstrated the capability of onboard processing from image data to wave spectra, which also significantly reduces data storage requirements [*Monaldo and Beal*, 1996].

This case study indicates the feasibility of using SAR in the advanced warning of high swell, which could also be crucial to the safety of offshore operations and coastal regions. Such a system is feasible with current spaceborne SARs for demonstration purposes at least and operationally in the future with improved ocean coverage and potentially onboard processing. In addition, combining improvements in high-swell prediction with storm surge modeling could also improve the prediction of water run-up in the coastal zone [*Bode and Hardy*, 1997].

Appendix A: Environmental Conditions for Validation of ERS-1 SAR Data With Buoy Data

A brief summary is provided of the weather and wave environment for each of the 10 dates used in the buoy-SAR validation (Table 1) based on NMC surface charts, site descriptions [*Galbraith et al.*, 1994], and buoy and wave model results.

A1. NDBC Buoy 46001

A1.1. September 18. On September 17 and 18 a low-pressure system to the west gradually moved northwestward and weakened later on September 18. Conditions were mild near the buoy until midday when a weak low-pressure system south and east of the buoy developed. The buoy measured wind speeds near 10 m s^{-1} with a wind direction from about 270° at midday, which gradually shifted to easterly during September 19 because of the front. H_s was near 3 m. The wave model indicated a wave direction from 230°. The SAR spectra showed a very consistent peak wavelength at 179 m from around 250°, from the low-pressure system to the west, and a less energetic peak of about 300 m from the north, with the latter related to the closer system. This lower frequency peak was not seen on the buoy frequency spectra and may have been nonlinearly mapped to a lower wavenumber on the SAR spectra since it had a strong radial component nearly parallel to the flight direction.

A1.2. October 15. No significant pressure systems were present near the buoy for October 15. Winds had dropped slightly to 12 from 15 m s^{-1} the day before. Modeled wave direction is 140°. The frequency spectra had a dominant period of 10 s and H_s of about 4 m. The dominant peak on the SAR spectra was at 157 m from a direction of 265°. A less energetic and quite variable peak in the SAR spectra is at 196 m from 134°, which aligns with the wind direction. The 157-m wave field may have emanated from a large low-pressure system present far to the west. In summary, the lack of a significant pressure system has resulted in a variable wind sea on both the buoy and the SAR data, producing a somewhat confusing comparison. There appears to be nonlinear mapping on the SAR spectra, even though the winds are some 40° off of the flight direction, which would tend to reduce the azimuth spectral component.

A1.3. October 24. A stable high-pressure system south of Alaska resulted in a very mild period before and during October 24. Wind speeds were <5 m s^{-1}, H_s was 1 m, and wind direction was from 180°. The wave model hindcast indicated a wave direction also of 180°. The dominant peak in the SAR spectra has similar measurements of 100 m from the south. In this case, then, short wavelength azimuth-traveling waves were apparently accurately mapped on the SAR spectra, primarily because of the low H_s.

A1.4. November 2. A low-pressure system developed near the buoy during November 2, with two substantial low-pressure systems to the west and south. Wind speeds were steady before and during this day at about 10 m s^{-1} from the west. The frequency spectra showed a stable 12-s wave field, also from the west according to the wave model (Figure 2). H_s was high at around 4.5 m. The SAR spectra showed a very steady 215-m wave field from nearly due west, comparing quite favorably with the buoy data.

A1.5. December 29. The strong low-pressure system discussed here is the same storm used in the case study discussed in section 3. According to the surface synoptic weather analysis a low-pressure system developed near Japan on December 25, 1991, and moved rapidly eastward. By December 27 at 1200 UTC it was a 962-mbar storm near the date line. At 0000 UTC on December 28 the intensive storm had matured with a center pressure of 954 mbar, shifting northeastward (about 60°) to a

position of about 46°N, 179°E (Figure 5). The storm had begun to weaken and its forward speed began to decrease by 0000 UTC on December 29, finally passing very near buoy 46001 late on December 29, with a pressure on 984 mbar. The time series frequency spectra shows a peak with an increasing density coincident to the SAR data on December 29 at 2100 UTC, indicating a peak of around 20 s (Figure 8). The model wave direction is from 300°, although the wind direction is generally from the west. The SAR spectra is quite comparable at 565 m, with a direction rotated slightly southward of the wind direction.

A2. ASREX Seatex Buoy

A2.1. November 4. A weak high-pressure system passed by the mooring in the early part of the day, when the westerly winds dropped from 10 to 3–4 m s^{-1} by about 0800 UTC. Later in the day, a weak low-pressure system arose, which increased wind speeds to 9–10 m s^{-1} and shifted the wind direction to southerly. Wave heights remained constant at around 3–3.5 m, with the dominant low-frequency peak emanating from a westerly direction of between 255° and 270°, having been generated from a strong low-pressure system well to the west. These waves are orthogonal or range traveling relative to the ERS-1 flight direction of 196°. Thus these waves are not subject to nonlinear SAR mapping conditions, and the buoy and SAR measurements are comparable.

A2.2. November 16. A strong storm system passed over the mooring during the middle of this day, reaching a low of about 968 mbar near midday. This was followed at 1800 UTC by peak winds of 22 m s^{-1} and H_s of 10 m with a maximum period of about 14–15 s. Earlier in the day, there was evidence of three wave systems: a low-frequency system propagating from the west with about a 14-s period, a 12-s period from the south, and a wind sea from the southeast. With the storm, the wind sea and low-frequency peaks steadily coalesced from a direction of about 240°. NMC surface charts showed the center of the low at 49°N, 136°W at 1200 UTC and 52°N, 133°W at 0000 UTC on November 17, some 250 km to the west of the buoy.

As noted in section 2, the SAR data showed considerably different dominant wave fields. The location of the SAR data is slightly east of the estimated storm center, between the storm and the buoy. There was a 195-m wave field with a propagation direction from 288° and a 536-m wave component propagating from 175°. The westerly SAR wave field is shorter than that measured by the buoy earlier in the day, and the southerly SAR wave field is considerably longer and rotated 60° toward the south from the dominant buoy component. Also, the steep wind waves in the SAR region are undoubtedly mapped in a nonlinear fashion on the imagery due to the strong wind component in the radial direction, nearly parallel to the flight direction, which resulted in a mapping to a lower wavenumber. The westerly wave component on the SAR imagery may be remaining from the earlier westerly component seen on the buoy data, although it is much shorter in wavelength. In conclusion, the strong rotating winds in the near field to the SAR likely produced nonlinear mapping of the wave field on the SAR spectra.

A2.3. November 25. At the time of the SAR overpass the wind speeds had dropped to around 5 m s^{-1} from the south from a high of 12 m s^{-1} from the west late on November 24. Wave heights are relatively constant at around 2–3 m. The low-frequency waves are propagating from the west. The SAR spectra is broad from the west, but the dominant lobe is centered at 307°. Thus, under these relatively mild conditions, the measured wavelengths are quite comparable, but the broad spectra results in a less accurate angular measurement.

A2.4. December 1. A high-pressure system has remained in the area for several days. A high wind speed of 14 m s^{-1} occurred at 1200 UTC from the northwest. Wave height remains around 3 m. The frequency spectra at the end of the day was unimodal at about 10 s with a directional peak at about 280°. The buoy and SAR comparisons are quite good.

A2.5. December 4. A front passed over the mooring late on December 3, with wind directions shifting from southerly to westerly. During December 4 the winds shifted slowly back to the south, with the wind speeds remaining steadily at 10 m s^{-1}. Wave height remains around 3–4 m. The low-frequency swell is from the west, while the higher-frequency waves track the wind. Again, the buoy and SAR comparisons of the dominant low-frequency waves are good.

Acknowledgments. The authors wish to thank C. Y. Peng and Y. Y. Chao of GSFC for their valuable discussions and suggestions; Ron Kwok, Glenn Cunningham, Amy Rodgers, and Joanne Shimada of JPL for development of the ASF geophysical processing system; and the ASF operational staff. The JPL effort was supported by the National Aeronautics and Space Administration through a contract with the Jet Propulsion Laboratory, California Institute of Technology. The GSFC work was supported by the National Aeronautics and Space Administration and Office of Naval Research. The ASREX program was supported by the Office of Naval Research under grant N00014-91J-1891.

References

Alpers, W. R., Monte Carlo simulations for studying the relationship between ocean waves and synthetic aperture radar image spectra, *J. Geophys. Res.*, *88*(C3), 1745–1759, 1983.

Barber, N. F., and F. Ursell, The generation and propagation of ocean waves and swell, *Philos. Trans. R. Soc. London A*, *240*, 527–560, 1948.

Beal, R. C. (Ed.), *Directional Ocean Wave Spectra*, 218 pp., Johns Hopkins Univ. Press, Baltimore, Md., 1991.

Beal, R. C., T. W. Gerling, D. E. Irvine, F. M. Monaldo, and D. G. Tilley, Spatial variations of ocean wave directional spectra, *J. Geophys. Res.*, *91*(C2), 2433–2449, 1986.

Bode, L., and D. A. Hardy, Progress and recent development in storm surge modeling, *J. Hydraul. Eng.*, *123*, 316–331, 1997.

Chen, H. S., Ocean surface waves, *Tech. Procedures Bull., Ser. 426*, 20 pp., Off. of Meteorol., Natl. Weather Serv., Natl. Oceanic and Atmos. Admin., 1995a.

Chen, H. S., Evaluation of a global ocean wave model at the National Meteorological Center, in *Proceedings of the Second International Conference on Hydro-Science and -Engineering, March 23–26, 1995, Beijing, China*, pp. 1436–1443, Tsinghua Univ. Press, Beijing, 1995b.

Dobson, F. W., and P. W. Vachon, The Grand Banks ERS-1 SAR wave spectra validation experiment, *Atmos. Ocean*, *32*(1), 7–29, 1994.

Earle, M. D., K. A. Bush, and G. D. Hamilton, High-height long-period ocean waves generated by a severe storm in the northeast Pacific Ocean during February 1983, *J. Phys. Oceanogr.*, *14*, 1286–1299, 1984.

Engen, G., H. Johnsen, H. E. Krogstad, and S. F. Barstow, Directional wave spectra by inversion of ERS-1 synthetic aperture radar ocean imagery, *IEEE Trans. Geosci. Remote Sens.*, *GE-32*, 340–352, 1994.

Galbraith, N. R., A. Gnanadesikan, G. H. Tupper, and B. S. Way, Meteorological and oceanographic data collected during the ASREX 91 field experiment, *Tech. Rep. 94-1*, 114 pp., Woods Hole Oceanogr. Inst., Woods Hole, Mass., 1994.

Gonzalez, F. I., B. Holt, and D. G. Tilley, The age and source of ocean swell observed in hurricane Josephine, Johns Hopkins *APL Tech. Dig.*, *8*, 94–99, 1987.

Hasselmann, K., and S. Hasselmann, On the nonlinear mapping of an

ocean wave spectrum into a synthetic aperture radar image spectrum and its inversion, *J. Geophys. Res.*, *96*(C6), 10,713–10,729, 1991.

Hasselmann, K., R. K. Raney, W. J. Plant, W. Alpers, R. A. Shuchman, D. R. Lyzenga, C. L. Rufenach, and M. J. Tucker, Theory of synthetic aperture radar ocean imaging: A MARSEN view, *J. Geophys. Res.*, *90*(C3), 4659–4686, 1985.

Hasselmann, S., C. Brüning, K. Hasselmann, and P. Heimbach, An improved algorithm for the retrieval of ocean wave spectra from synthetic aperture radar image spectra, *J. Geophys. Res.*, *101*(C7), 16,615–16,629, 1996.

Holt, B., and F. I. Gonzalez, SIR-B observations of dominant ocean waves near Hurricane Josephine, *J. Geophys. Res.*, *91*(C7), 8595–8598, 1986.

Janssen, P. A. E. M., Wave-induced theory of wind-wave generation applied to wave forecasting, *J. Phys. Oceanogr.*, *19*, 745–754, 1989.

Janssen, P. A. E. M., Quasi-linear theory of wind-wave generation applied to wave forecasting, *J. Phys. Oceanogr.*, *21*, 1631–1642, 1991.

Kleijweg, J. C. M., and H. Greidanus, Validation of directional wave spectra from the ERS-1 during the ESA Cal/Val campaign, in *Proceedings of the First ERS-1 Symposium, Cannes, France, 4–6 November 1992, Eur. Space Agency Spec. Publ., ESA SP-359*, 31–34, 1993.

Komen, G. J., L. Cavalieri, M. Donelan, K. Hasselman, S. Hasselmann, and P. A. E. M. Janssen, *Dynamics and Modeling of Ocean Waves*, 532 pp., Cambridge Univ. Press, New York, 1994.

Krogstad, H. E., A simple derivation of Hasselmann's nonlinear ocean–synthetic aperture radar transform, *J. Geophys. Res.*, *97*(C2), 2421–2425, 1992.

Krogstad, H. E., O. Samset, and P. W. Vachon, Generalizations of the non-linear ocean-SAR transform and a simplified SAR inversion algorithm, *Atmos. Ocean*, *32*(1), 61–82, 1994.

McLeish, W., and D. B. Ross, Imaging radar observations of directional properties of ocean waves, *J. Geophys. Res.*, *88*(C7), 4407–4419, 1983.

Mettlach, T., D. Wang, and P. Wittman, Analysis and prediction of ocean swell using intrumented buoys, *J. Atmos. Oceanic Technol.*, *11*(2), 506–524, 1994.

Monaldo, F. M., The consequences of sampling variability on the estimation of wave number and propagation direction from spaceborne SAR image spectra, *IEEE Trans. Geosci. Remote Sens.*, *GE-29*, 113–119, 1991.

Monaldo, F. M., and R. C. Beal, Comparison of wave parameters measured from the SIR-C on-board processor with WAM predictions in the Southern Ocean, *Rep. SIR-96-01*, 37 pp., Johns Hopkins Univ., Laurel, Md., 1996.

Monaldo, F. M., T. G. Gerling, and D. G. Tilley, Comparison of SIR-B SAR wave image spectra with wave model predictions: Implications on the SAR modulation transfer function, *IEEE Trans. Geosci. Remote Sens.*, *GE-31*, 1199–1209, 1993.

Munk, W. H., G. R. Miller, F. E. Snodgrass, and N. F. Barber, Directional recordings of swell from distant storms, *Philos. Trans. R. Soc. London A*, *255*, 505–583, 1963.

National Oceanic and Atmospheric Administration, North Pacific weather: October, November, and December 1991, *Mar. Weather Log*, *36*(2), 72–85, 1992.

Overland, J. E., and T. R. Heister, Development of a synoptic climatology for the northeast Gulf of Alaska, *J. Appl. Meteorol.*, *19*, 1–14. 1980.

Plant, W. J., Reconciliation of theories of synthetic aperture radar imagery of ocean waves, *J. Geophys. Res.*, *97*(C5), 7493–7501, 1992.

Plant, W. J., and L. M. Zurk, Dominant wave directions and significant wave heights from synthetic aperture radar imagery of the ocean, *J. Geophys. Res.*, *102*(C2), 3473–3482, 1997.

Raney, R. K., SAR response to partially coherent phenomena, *IEEE Trans. Antennas Propag.*, *AP-26*, 777–787, 1980.

Sea Wave Modeling Project (SWAMP) Group, *Ocean Wave Modeling*, 262 pp., Plenum, New York, 1985.

Shearman, R. J., and A. A. Zelenko, Wind measurements reduction to a standard level, *Mar. Meteorol. and Relat. Oceanogr. Activ. Rep. 22*, 30 pp., World Meteorol. Organ., Geneva, 1989.

Snodgrass, F. E., G. W. Groves, K. F. Hasselmann, G. R. Miller, W. H. Munk, and W. H. Powers, Propagation of ocean swell across the Pacific, *Philos. Trans. R. Soc. London A*, 431–497, 1966.

Snyder, J. P., Map projections: A working manual, *U.S. Geol. Surv. Prof. Pap.*, *1395*, 383 pp., 1987.

Stern, H. L., D. A. Rothrock, R. Kwok, and B. Holt, The geophysical processor system: Automated analysis of ERS-1 SAR imagery, in *Proceedings of the Second ERS-1 Symposium, Hamburg, Germany, 11–14 October 1993*, Eur. Space Agency Spec. Publ., *ESA SP-361*, 281–286, 1994.

Tilley, D. G., and R. C. Beal, ERS-1 and Almaz estimates of directional wave spectra conditioned by simultaneous aircraft SAR and buoy measurements, *Atmos. Ocean*, *32*(1), 113–142, 1994.

Vachon, P. W., H. E. Krogstad, and J. S. Paterson, Airborne and spaceborne synthetic aperture radar observations of ocean waves, *Atmos. Ocean*, *32*(1), 83–112, 1994.

Wadhams, P., and B. Holt, Waves in frazil and pancake ice and their detection in Seasat synthetic aperture radar imagery, *J. Geophys. Res.*, *96*(C5), 8835–8852, 1991.

Wang, D. W., and R. Carolan, Estimation of swell direction by a small discus buoy in high seas, in *Proceedings of the Fifth Conference on Meteorology and Oceanography of the Coastal Zone Miami, Fla., May 6–9, 1991*, pp. 53–59, Am. Meteorol. Soc., Boston, Mass., 1991.

Wave Model Development and Implementation (WAMDI) Group, The WAM model: A third generation ocean wave prediction model, *J. Phys. Oceanogr.*, *18*, 1775–1810, 1988.

H. S. Chen, National Centers for Environmental Prediction, NOAA, Washington, DC 20233.

A. Gnanadesikan, Program in Atmospheric and Oceanic Sciences, Princeton University, Princeton, NJ 08540.

B. Holt, Jet Propulsion Laboratory, California Institute of Technology, 4800 Oak Grove Drive, Pasadena, CA 91109-8099. (e-mail: ben@pacific.jpl.nasa.gov)

A. K. Liu, Oceans and Ice Branch, NASA Goddard Space Flight Center, Greenbelt, MD 20771.

D. W. Wang, Applied Technology Division, Computer Sciences Corporation, Stennis Space Center, MS 39529.

(Received February 5, 1997; revised August 21, 1997;
accepted September 8, 1997.)